Journal of Materials Chemistry A

ROYAL SOCIETY OF CHEMISTRY

PAPER

View Article Online
View Journal | View Issue

Cite this: J. Mater. Chem. A, 2024, 12, 16877

Experimental and theoretical investigation on facet-dependent MoO_2/BiOBr Z-scheme heterojunction photocatalytic nitrogen reduction: modulation of bulk charge separation efficiency by built-in electric field intensity†

Zhuying Chen,[a] Zhiling Huang,[b] Jieyi Yang,[a] Yue Meng,[b] Bo Xie,[a] Zheming Ni[a] and Shengjie Xia *[a]

Based on facet engineering and Z-scheme heterojunctions, a series of MoO_2/BiOBr Z-scheme heterojunctions with different facet ratios of (102)/(001) were prepared for photocatalytic nitrogen reduction. The performance of nitrogen reduction is greatly improved after constructing heterojunctions, and the activity increases rapidly with the increase of the (102)/(001) ratio of BiOBr in the heterojunction. MoO_2/BiOBr-0 with a (102)/(001) ratio of 0.167 exhibits the highest activity, reaching 176.66 μmol g^{-1} h^{-1}, which is 4–5 times higher than that of pristine MoO_2 and BiOBr. Based on the built-in electric field (BIEF) strength, bulk charge separation (BCS) efficiency, and theoretical calculation of the materials, it is believed that due to the increase in the (102)/(001) facet ratio, the BIEF strength between the two phases of the heterojunction is enhanced, resulting in a high BCS efficiency. This promotes more surface enriched photo-generated electrons to act on nitrogen reduction, thereby achieving efficient photocatalytic ammonia synthesis. According to DFT, compared to MoO_2 and BiOBr, MoO_2/BiOBr not only adsorbs N_2 more strongly than H, but also ΔG_{max} in the potential energy determination step (PDS) is lower, thus exhibiting superior NRR activity. The calculation is completely consistent with the experimental results, further confirming that the construction of Z-scheme heterojunctions with a high proportion of (102) facets greatly promotes the performance of MoO_2 and BiOBr in catalyzing nitrogen reduction.

Received 8th April 2024
Accepted 3rd June 2024

DOI: 10.1039/d4ta02394c

rsc.li/materials-a

1. Introduction

Ammonia (NH_3) plays a crucial role in industries such as fertilizers, pharmaceuticals, daily chemicals, and energy. Currently, the production of ammonia in industry relies on the high-temperature and high-pressure Haber–Bosch process, which accounts for approximately 2% of global energy consumption and generates approximately 1.6% of global greenhouse gas emissions.[1–3] Therefore, driving nitrogen reduction to synthesize ammonia under mild conditions has important scientific significance and significant application value. However, the inert molecular structure of N_2 and the high dissociation energy of N≡N bonds, as well as the presence of high-energy intermediates such as N_2H, greatly hinder its activation and selective transformation at room temperature and pressure.[4–6] By using appropriate catalysts in conjunction with energy such as light and electricity, the nitrogen reduction pathway can be changed, promoting nitrogen dissociation and making the ammonia synthesis process less or less restricted by thermodynamic equilibrium.[7–9] Thus, photocatalytic nitrogen reduction is considered a potential method to replace the industrial Haber–Bosch process for generating ammonia.

Photocatalytic nitrogen reduction, with the assistance of light, converts nitrogen and water into ammonia, which has significant advantages:[10,11] (1) low energy consumption, as it uses clean solar energy as the energy source; (2) mild reaction conditions, allowing it to be carried out at room temperature and pressure; (3) environmental friendliness, as it replaces non-renewable fossil fuels with water as a hydrogen source, reducing CO_2 gas emissions.[12] The currently researched nitrogen reduction photocatalysts mainly include single atom and cluster catalysts,[13] transition metal oxides (TiO_2 and WO_x),[14,15] nitrides (C_xN and BN),[16,17] metal sulfides (MoS_2 and $ZnIn_2S_4$),[18,19] metal oxygenates (Bi_2MoO_6),[20] and metal–organic frameworks

[a]Department of Chemistry, College of Chemical Engineering, Zhejiang University of Technology, Hangzhou 310014, P. R. China. E-mail: xiasj@zjut.edu.cn; Tel: +86-571-88320373

[b]Department of Pharmaceutical Engineering, School of Life and Health Sciences, Huzhou College, Huzhou 313000, P. R. China

† Electronic supplementary information (ESI) available. See DOI: https://doi.org/10.1039/d4ta02394c

(MOFs).[21] Although there has been some research progress in photocatalytic ammonia synthesis, it still faces difficulties and challenges, mainly due to the low charge separation efficiency of semiconductor catalysts, resulting in low energy conversion efficiency, and the difficulty in activating nitrogen, resulting in a small number of activated molecules participating in the ammonia synthesis reaction.

Facet engineering is currently one of the important strategies to improve the charge separation efficiency of photocatalysts.[22] By selectively exposing specific crystal planes through facet regulation, a cascade band structure can be formed between co-exposed facets with anisotropy, driving efficient directional migration and separation of photo-generated electrons and holes. Meanwhile, the selectively exposed facets in photocatalysts can provide active sites/planes for photocatalytic reactions or the loading of co-catalysts, resulting in facet dependence in photocatalytic reactions.[23] For example, the (110) surface of Cu_2O single crystals exhibits photocatalytic activity for CO_2 reduction to methanol, while the (100) surface exhibits inertness.[24] The photogenerated electrons and holes generated by Bi_3O_4Cl under photoexcitation tend to aggregate on the (110) and (010) surfaces, respectively. That is, the (110) surface of Bi_3O_4Cl tends to undergo the oxygen evolution reaction, while the (010) surface tends to undergo the hydrogen evolution reaction.[25]

Although facet regulation can achieve directional separation of photo-generated charge carriers and inhibit their surface recombination, its effect is still limited in addressing the problem of an insufficient number of activated molecules involved in ammonia synthesis due to the difficulty of nitrogen activation. Building heterojunctions is an effective means.[26] A Z-scheme heterojunction (also known as the S-scheme) is a typical example, where the built-in electric field between the two phases can accelerate the separation and transfer of charge carriers, allowing electrons to accumulate at high energy levels and holes to accumulate at low energy levels, greatly maintaining the redox energy of the photocatalyst.[27,28] For example, Lam and Liu *et al.* used 0D $AgInS_2$ nanoparticles and 2D MXene (Ti_3C_2) nanosheets to construct a Z-scheme heterostructure with good interfacial charge transfer ability.[29] The yield of ammonia synthesis by nitrogen reduction under visible light irradiation can reach 38.8 μmol g^{-1} h^{-1}. Zhang *et al.* prepared $BiVO_4/S_V$-$ZnIn_2S_4$ Z-scheme heterojunction photocatalysts containing S vacancies, and the built-in electric field formed between the two phases assisted the ammonia generation rate to reach 58.5 μmol g^{-1} h^{-1}, which is 2.8 times and 3.3 times higher than that of $BiVO_4$ and $ZnIn_2S_4$, respectively.[30]

Thus, combining facet regulation and Z-scheme heterojunctions, constructing a class of Z-scheme heterojunctions with different facet ratios, is expected to alleviate the problems of low charge separation efficiency and a small number of activated molecules faced by current nitrogen reduction photocatalysts. The selection of Z-scheme heterojunction phases with different facet ratios is crucial. Halogenated oxides (AOX (A = Bi, La, *etc.*; X = Cl, Br, I)) are tetragonal crystal systems that typically have a regular polycrystalline plane structure. They not only have large specific surfaces, multiple active centers, and controllable energy bands, but also have advantages such as high chemical stability and low toxicity. More importantly, their conduction band bottom is higher than the nitrogen reduction potential (N_2/NH_3 = −0.0922 eV, NHE), making them very suitable for the pNRR.[31] Nano-MoO_2 has advantages such as strong chemical and photostability, small and regular particle size, narrow bandgap, high (negative) conduction band potential, and strong reduction ability. It is applied in various photocatalytic reduction reactions and is an ideal material for constructing heterojunctions.[32]

In summary, in this paper, a series of Z-scheme heterojunctions with adjustable crystal faces of BiOBr and MoO_2 were prepared for photocatalytic nitrogen reduction synthesis of ammonia. The activity, stability, and reusability of MoO_2/BiOBr Z-scheme heterojunctions with different (102)/(001) ratios for photocatalytic nitrogen reduction were systematically discussed. The Z-scheme electron transfer mechanism of the heterojunction was verified by characterizing free radicals, analyzing the band structure of the catalyst, and combining XPS and differential charge density. The built-in electric field strength and bulk charge separation efficiency of heterojunctions were investigated using surface photovoltage spectroscopy and transient fluorescence spectroscopy characterization. Finally, the energy barriers of the reaction pathways and rate-determining steps of MoO_2, BiOBr and MoO_2/BiOBr heterojunction catalytic nitrogen reduction were analyzed and compared through theoretical calculations, and a detailed mechanism analysis was finally provided.

2. Experimental

The details of the reagents, material characterization, and nitrogen reduction experiments are listed in the ESI.†

2.1. Preparation of BiOBr nanosheets (conventional thickness)

Firstly, 1 mmol of $Bi(NO_3)_3 \cdot 5H_2O$ was added to two beakers containing 15 mL of distilled water and stirred for 30 minutes. Secondly, 2 mmol of potassium bromide was dissolved in 30 mL of distilled water, divided into two equal parts, and then added dropwise to the above solution to obtain a mixed solution. The pH was adjusted to 2 and 1 using a sodium hydroxide solution (1 M) or nitric acid solution (1 M). The mixture was transferred to a 50 mL PTFE lined stainless steel high-pressure vessel and heated at 220 °C for 24 hours. It was cooled naturally to room temperature, washed 3 times with deionized water and 2 times with ethanol, and dried overnight at 60 °C to obtain catalysts named BiOBr-1 and BiOBr-2.

2.2. Preparation of BiOBr nanosheets (ultrathin)

Firstly, 1.0 mmol $Bi(NO_3)_3 \cdot 5H_2O$ was dissolved in 25 mL of 0.1 M mannitol solution and stirred for 10 minutes. Then, 5 mL of saturated potassium bromide solution was slowly added to obtain a uniform white suspension and stirred for 10 minutes. Subsequently, it was transferred to a 100 mL PTFE lined stainless steel high-pressure vessel and heated at 160 °C for 3 hours.

It was washed several times with deionized water and ethanol and the solid powder obtained was collected by centrifugation. Finally, it was dried at 60 °C for 4 hours to obtain the catalyst named BiOBr-0.

2.3. Preparation of MoO_2/BiOBr heterojunctions

0.009 mmol (0.11 g) ammonium molybdate tetrahydrate was dispersed in 30 mL of distilled water, stirred at room temperature for 30 minutes, and then 8 mL of ethylene glycol was added dropwise into the solution and stirred at room temperature for 30 minutes. Under stirring, 0.328 mmol (0.1 g) of BiOBr-0, BiOBr-1, and BiOBr-2 was dispersed in the above solution and stirred at room temperature for 10 minutes. Then all the solution was poured into a 100 mL PTFE lined stainless steel high-pressure vessel and heated in water at 180 °C for 36 hours. After the reaction was completed, the reactor was cooled to room temperature. The reaction solution was washed three times with ethanol and distilled water and vacuum dried at 60 °C for 4 hours to obtain bismuth bromide supported molybdenum oxide photocatalysts (MoO_2/BiOBr-0, MoO_2/BiOBr-1, and MoO_2/BiOBr-2).

2.4. DFT calculation parameters

The model and parameter settings for DFT calculation can be found in the ESI.† Among them, the BiOBr (001) crystal plane is constructed from optimized BiOBr units, while the MoO_2 (001) crystal plane is constructed from optimized MoO_2 units, as shown in Fig. S3.†

3. Results and discussion

3.1. Structure and morphology analysis

In order to analyze the microstructure and elemental composition of the MoO_2/BiOBr-0 catalyst, SEM, TEM, HRTEM, and EDX element mapping were used for characterization. From the SEM images (Fig. 1a) and TEM images (Fig. 1b) of BiOBr-0, it can be seen that its morphology is a sheet-like structure. The high-resolution electron microscopy (HRTEM) image (Fig. 1c) clearly shows that the lattice stripe spacing of 0.284 nm represents the (102) crystal plane of BiOBr-0.[33] The morphology of MoO_2 is spherical (Fig. 1d), and the crystal plane with lattice stripes of 0.246 nm represents the (200) plane of MoO_2 (Fig. 1e).[34] In the SEM image of MoO_2/BiOBr-0 (Fig. 1f), it is clear that MoO_2 spherical particles are interspersed on the sheet-like structure of BiOBr-0, and the distribution of the two phases can also be seen in the TEM image of MoO_2/BiOBr-0 (Fig. 1g). In addition, clear lattice stripes and two-phase interfaces can be seen from the HRTEM images of MoO_2/BiOBr-0 (Fig. 1h), indicating that the catalyst has good crystallinity. The lattice stripes of 0.284 nm and 0.352 nm correspond to the (102) crystal plane of BiOBr-0 and the (−111) crystal plane of MoO_2, respectively. The above results confirm the synthesis of the MoO_2/BiOBr heterojunction. Moreover, the EDX element map of MoO_2/BiOBr-0 shows a uniform distribution of Bi, Br, O, and Mo elements (Fig. 1i).

The crystal structure of the catalysts was further confirmed through XRD (Fig. 2a). Clear diffraction peaks of (001), (102), (110), and (200) crystal planes were observed in pristine BiOBr, consistent with JCPDS cards 73-2061.[35] The characteristic diffraction peaks in pure phase MoO_2 correspond to the (−111) and (−312) facets of JCPDS card 32-0671, respectively. The characteristic diffraction peaks of BiOBr and MoO_2 simultaneously appear in MoO_2/BiOBr-0, proving the successful synthesis of the MoO_2/BiOBr heterojunction.[36] In addition, X-ray photoelectron spectroscopy (XPS) was used to characterize the elemental composition of the composite catalyst. The results are shown in Fig. 2b, and diffraction peaks corresponding to Bi, Mo, and O appeared in MoO_2/BiOBr-0, indicating the formation of a tight heterojunction interface between BiOBr and MoO_2, which is conducive to charge transfer within the catalyst.

3.2. Photoelectric performance analysis

The optical properties of the catalyst were investigated using UV visible diffuse reflectance spectroscopy (UV-vis DRS), and the results are shown in Fig. 2c. It can be seen that the visible light absorption edge of pristine BiOBr is around 440 nm, while MoO_2 does not have a clear visible light absorption edge. This may be due to the narrow bandgap of MoO_2, which does not have a clear gap between its conduction band and valence band. The light absorption ability of the catalyst after BiOBr and MoO_2 complex formation is greatly improved in the visible light region of 400–800 nm, especially for MoO_2/BiOBr-0, which expands its visible light response range to about 750 nm. This indicates that when BiOBr is modified with MoO_2 with surface plasmon resonance, its visible light absorption range is significantly improved. Meanwhile, the visible light absorption intensity of the heterojunction has also been greatly enhanced.[37] The bandgap of BiOBr and MoO_2 can be calculated using the Kubelka–Munk function (1):

$$(\alpha h\nu) = A(h\nu - E_g)^{n/2} \quad (1)$$

where α is the light absorption coefficient, $h\nu$ is the photon energy, and A is the Planck constant. As shown in Fig. 2d, the bandgap of BiOBr and MoO_2 is 2.72 eV and 2.24 eV, respectively.

The separation of photo-generated carriers in the catalyst was characterized through transient photocurrent and electrochemical impedance spectroscopy (EIS). Fig. 2e shows the transient photocurrent results of BiOBr, MoO_2, and MoO_2/BiOBr-0. It can be seen that MoO_2/BiOBr-0 exhibits the maximum photocurrent response. Meanwhile, electrochemical impedance characterization shows that MoO_2/BiOBr-0 also exhibits the minimum interface impedance, indicating that it has the highest photo-generated electron–hole separation efficiency (Fig. 2f).

Based on the above analysis, it is demonstrated that the obtained MoO_2/BiOBr-0 has good visible light utilization efficiency and photo-generated electron–hole separation efficiency.

3.3. Exploration of the facet ratio for BiOBr nanosheets

The crystal structure of BiOBr nanosheets with different facet ratios was studied by X-ray diffraction (XRD) and scanning

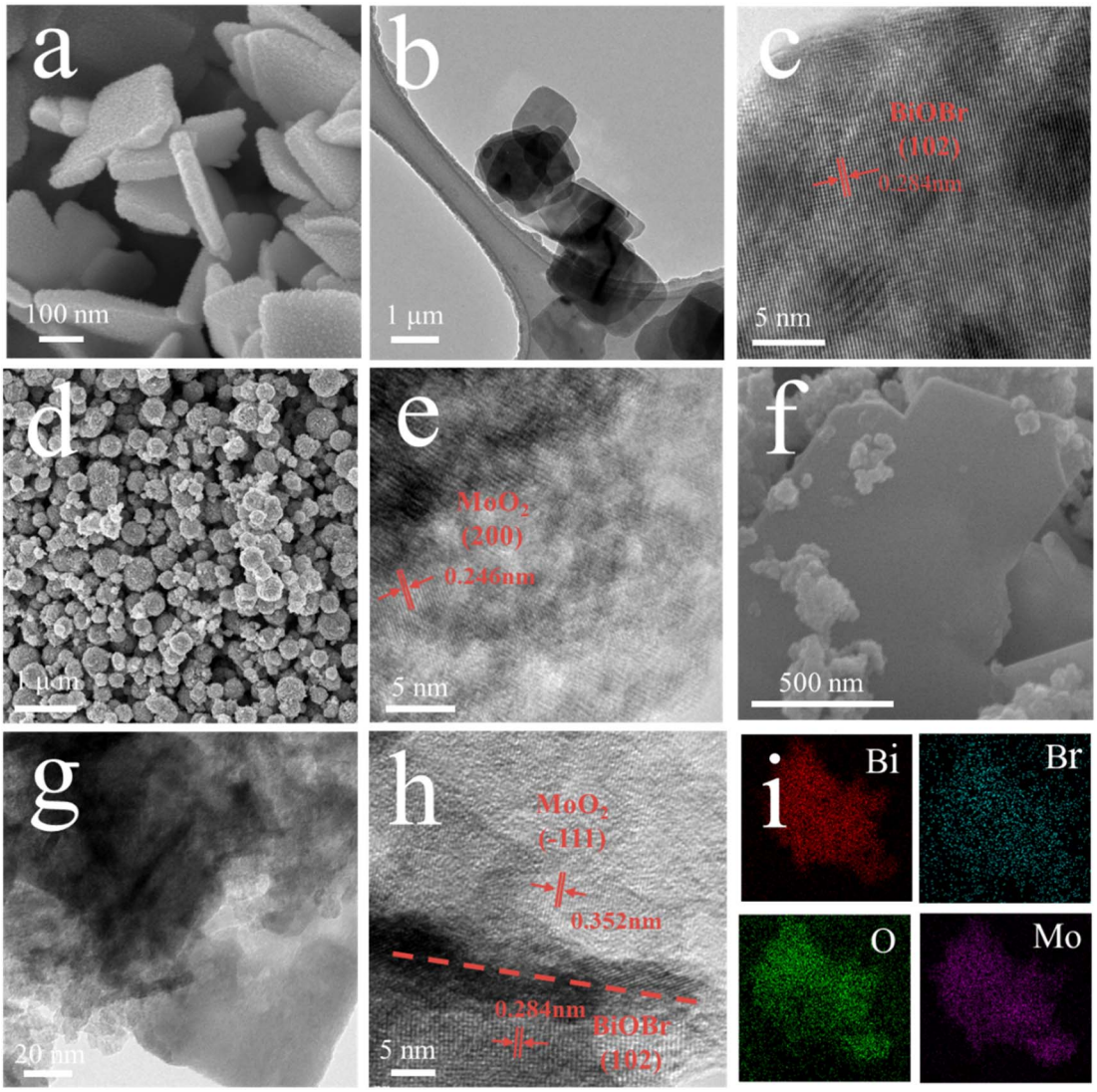

Fig. 1 (a) SEM image of BiOBr-0; (b) TEM image of BiOBr-0; (c) HRTEM image of BiOBr-0; (d) SEM image of MoO_2; (e) HRTEM image of MoO_2; (f) SEM image of MoO_2/BiOBr-0; (g) TEM image of MoO_2/BiOBr-0; (h) HRTEM image of MoO_2/BiOBr-0; (i) element mapping of MoO_2/BiOBr-0.

electron microscopy (SEM). Fig. 3a shows that the XRD patterns of all materials are consistent with the JCPDS cards 73-2061 of BiOBr, in which BiOBr-2, BiOBr-1, and BiOBr-0 all have higher exposed (001) and (102) surfaces.[38] The SEM images (Fig. 3b–d) indicate that BiOBr nanosheets are all square in shape, but the size of the nanosheets has changed. Fig. 3f–h show that the nanosheets of BiOBr-2, BiOBr-1, and BiOBr-0 have thicknesses of 347 nm, 133 nm, and 37 nm, respectively. According to the formula for calculating the ratio of crystal planes in Fig. 3e, it was found that the facet ratio of (102)/(001) of BiOBr-2, BiOBr-1, and BiOBr-0 is 0.011, 0.053, and 0.167, which is continuously increasing. This means that by adjusting the overall particle size of the BiOBr crystal plane, the exposure of the (102) side continuously increases (Fig. 3i–k).

The deposition of Ag ($Ag^+ + e^- = Ag$) on the side of BiOBr has been demonstrated through photo-deposition experiments (Fig. S4†), and the literature has also reported that Pt and Au can be deposited on the side of BiOBr, while MnO_x can be deposited on the front.[39] That is to say, the (001) surface of BiOBr is conducive to the deposition of holes as an oxidized active surface, while the (102) surface is conducive to the deposition of electrons as a reduced active surface. Therefore, in materials with different facet ratios, BiOBr-0 with the highest (102)/(001) facet ratio may have higher reduction efficiency. The SEM images of heterojunctions constructed from BiOBr and MoO_2 with different facet ratios are shown in Fig. 4a–c, indicating that MoO_2 has been successfully loaded onto BiOBr-2, BiOBr-1, and BiOBr-0 nanosheets.

3.4. Photocatalytic nitrogen reduction by MoO_2/BiOBr with different facet ratios

The experimental results of photocatalytic synthesis of ammonia are shown in Fig. 4d. Under visible light irradiation, the activity of different catalysts is MoO_2/BiOBr-0 (176.66 μmol g^{-1} h^{-1}) > MoO_2/BiOBr-1 (70.85 μmol g^{-1} h^{-1}) > MoO_2/BiOBr-2 (61.23 μmol g^{-1} h^{-1}) > MoO_2 (40.57 μmol g^{-1} h^{-1}) > BiOBr

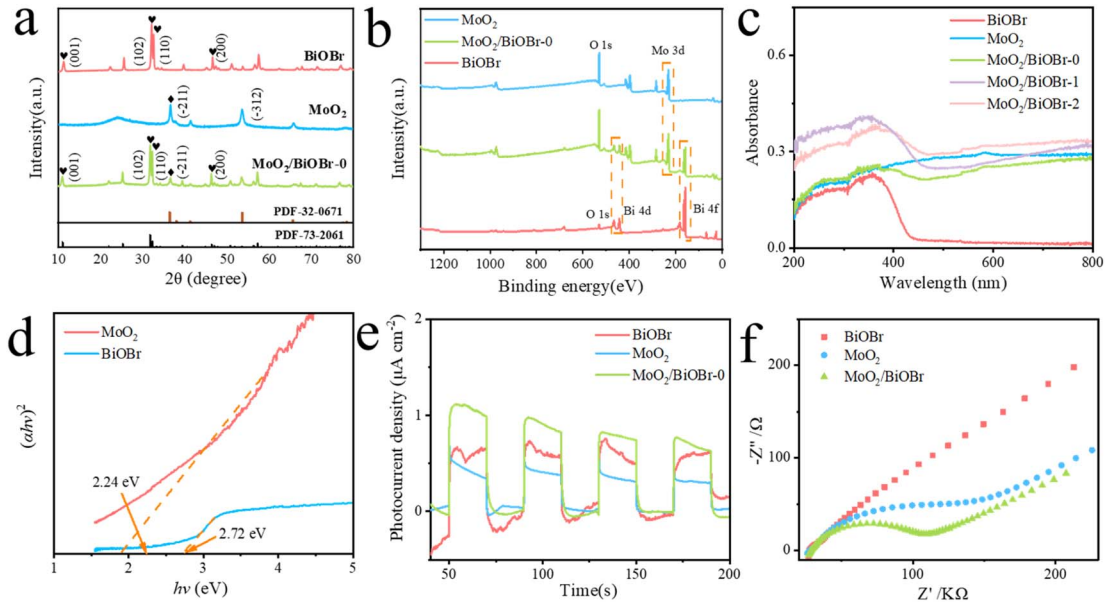

Fig. 2 The characterization of samples: (a) XRD pattern and (b) XPS full spectrum; (c) UV-vis diffuse reflectance spectra; (d) plots of $(\alpha hv)^2$ *vs. hv* for all samples; (e) transient photocurrent; (f) electrochemical impedance.

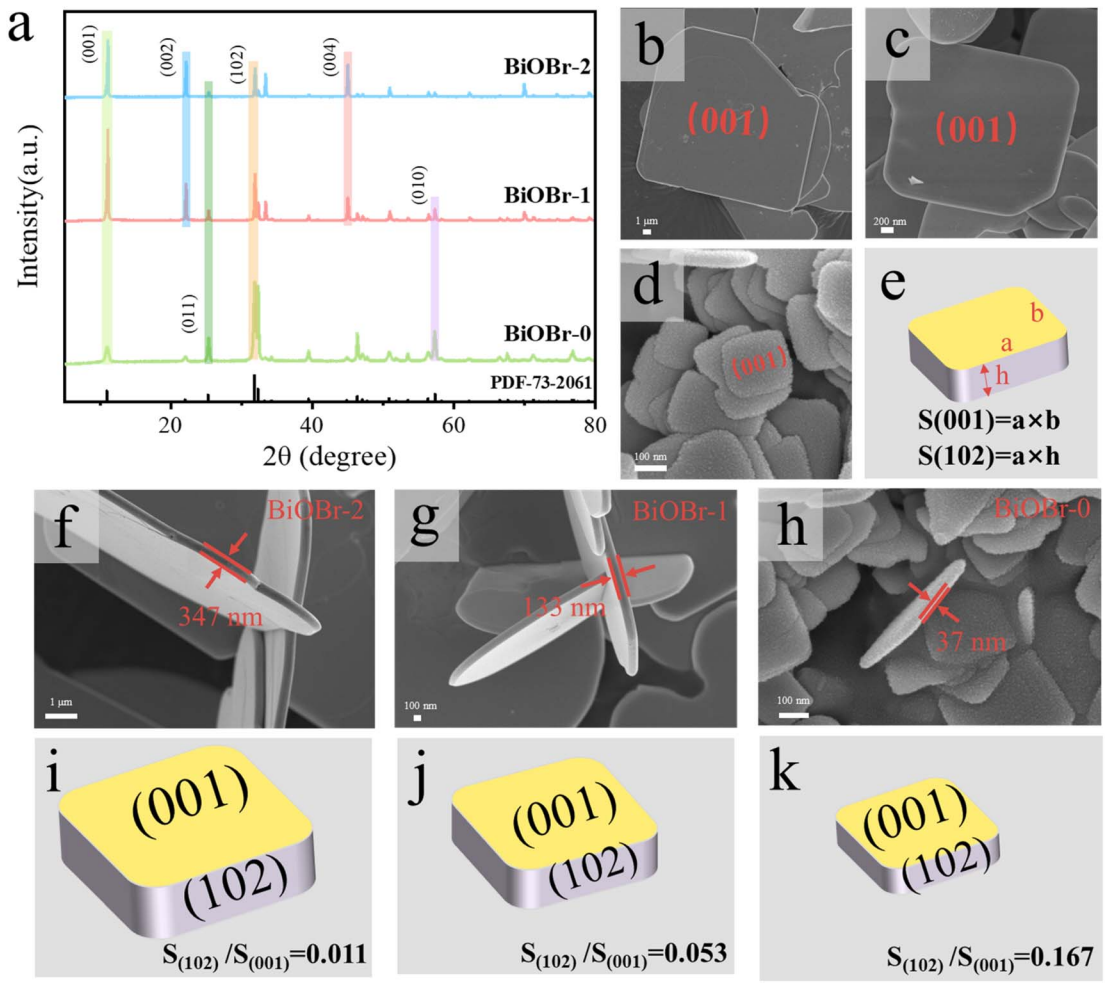

Fig. 3 Characterization of BiOBr nanosheets with different facet ratios: (a) XRD and SEM images of (b and f) BiOBr-2, (c and g) BiOBr-1 and (d and h) BiOBr-0; (e) schematic diagram of calculation formulae for different crystal face ratios; crystal ratio diagrams of (i) BiOBr-2, (j) BiOBr-1 and (k) BiOBr-0.

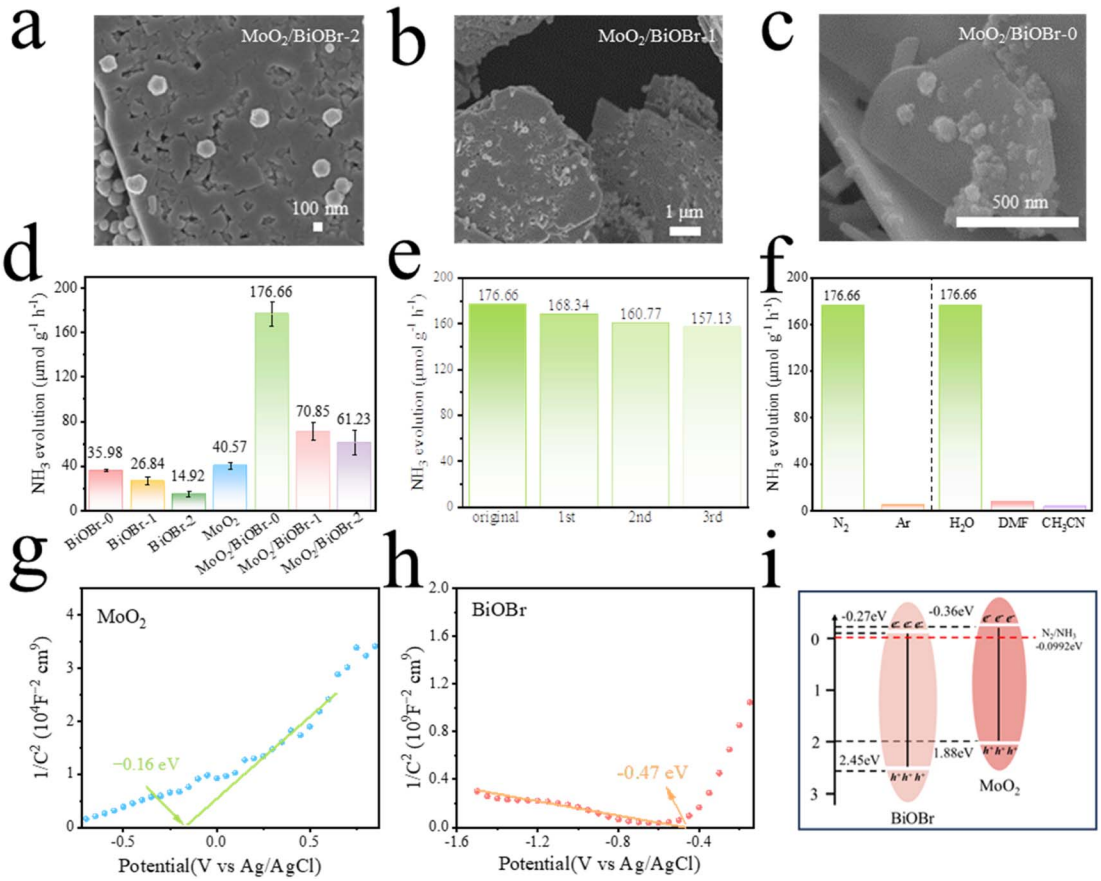

Fig. 4 SEM images of (a) MoO_2/BiOBr-2, (b) MoO_2/BiOBr-1 and (c)MoO_2/BiOBr-0; (d) nitrogen reduction yields of different catalysts under visible light; (e) the cycles of nitrogen reduction; (f) nitrogen reduction yield of the MoO_2/BiOBr catalyst in different atmospheres and solvents; Mott–Schottky of (g) BiOBr and (h) MoO_2; (i) the alignment of the band structure of MoO_2/BiOBr-0.

(35.98 μmol g^{-1} h^{-1}). MoO_2/BiOBr composites exhibit higher photocatalytic efficiency for ammonia synthesis than MoO_2 and BiOBr, which may be due to the higher visible light utilization efficiency and photo-generated carrier separation efficiency of the heterojunction compared to single-phase catalysts. Meanwhile, MoO_2/BiOBr-0 exhibited the highest photocatalytic activity for ammonia synthesis, which was 4.9 times and 4.3 times higher than that of pristine BiOBr and MoO_2, respectively. In addition, the NH_4^+ generation of all catalysts will increase with the extension of the ammonia synthesis experiment time (Fig. S5†), proving that the photocatalytic ammonia synthesis reaction has good stability. The reusability of the MoO_2/BiOBr-0 catalyst was further investigated, and the results showed that the performance of the catalyst did not significantly decrease after three cycles (Fig. 4e). Fig. 4f indicates that under an Ar atmosphere, the catalyst has almost no synthetic ammonia yield, indicating that the nitrogen in NH_4^+ mainly comes from N_2, and it is also evident that only ammonia is generated in H_2O solution, while there is almost no ammonia generated in DMF and CH_3CN solutions, indicating that the hydrogen in NH_4^+ mainly comes from H_2O.

In addition, $^{15}N_2$ was used for isotope labeling (Fig. S6†). When only argon was introduced, the NMR spectrum had no signal. When $^{14}N_2$ was introduced, since ^{14}N has a spin of 1, there can be three spin states (+1, 0, and −1), which makes the peak value become a triplet state with a coupling constant of 52 Hz.[40] When only $^{15}N_2$ was introduced, the resonance split into a double peak with a coupling constant of 72 Hz, because ^{15}N has a spin of 1/2, which shows spin–spin coupling.[41]

Moreover, XRD characterization of MoO_2/BiOBr-0 before and after reaction was performed and the results are given in Fig. S7.† It can be seen that the XRD curves of MoO_2/BiOBr-0 samples before and after the reaction are basically consistent, indicating that the material has good structural stability.

3.5. Mechanism of photocatalytic nitrogen reduction

3.5.1 Band structure of catalysts. By exploring the band structures of materials through Mott–Schottky spectroscopy, the Schottky curves of BiOBr and MoO_2 are shown in Fig. 4g and h. It can be seen that the flat band potentials of BiOBr and MoO_2 are −0.47 eV and −0.16 eV, respectively. Due to BiOBr being a p-type semiconductor and MoO_2 being an n-type semiconductor, the E_{CB} values of BiOBr and MoO_2 can be approximately −0.27 eV and −0.36 eV, respectively.[42] In addition, the E_{VB} of BiOBr and MoO_2 was calculated based on the formula $E_{VB} = E_{CB} + E_g$, and it was found that the E_{VB} of BiOBr and MoO_2 was approximately 2.45 eV and 1.88 eV, respectively, indicating that

the energy bands of the two were cross arranged (Fig. 4i). Thus, BiOBr and MoO_2 used for photocatalytic ammonia synthesis are thermodynamically feasible.[43]

3.5.2 Built-in electric field and Z-scheme heterojunction. In order to investigate the mechanism of the Z-scheme heterojunction, the catalyst was characterized by electron paramagnetic resonance (ESR). The results are shown in Fig. 5a–f. Under dark conditions, BiOBr, MoO_2 and MoO_2/BiOBr-0 did not produce DMPO–$\cdot O_2^-$ and DMPO–$\cdot$OH signals. After 10 minutes of illumination, MoO_2 and MoO_2/BiOBr-0 showed signals of DMPO–$\cdot O_2^-$, while BiOBr did not. For the signal of DMPO–$\cdot$OH, BiOBr and MoO_2/BiOBr-0 were generated after illumination, while MoO_2 was not. This indicates that the photo-generated electrons and holes in the MoO_2/BiOBr catalyst cluster on the conduction band of MoO_2 and the valence band of BiOBr, respectively. This transport mode follows the transport mechanism of the Z-scheme heterojunction, rather than the conventional type II heterojunction.[44]

Meanwhile, the work functions of BiOBr and MoO_2 were also calculated using DFT. As shown in Fig. 5g and h, the work functions of BiOBr and MoO_2 were 5.629 eV and 3.782 eV, respectively. The relationship between the Fermi level and the work function is given as formula (2):

$$E_F = E_{vac} - \Phi i \quad (2)$$

n which, E_F, E_{vac} and Φ are the Fermi level, work function, and vacuum level (usually 0). The Fermi levels (E_F) of BiOBr and MoO_2 were calculated to be −5.629 eV and −3.782 eV, respectively. It is evident that the Fermi level of BiOBr is lower than that of MoO_2. Thus, when two phases come into contact, due to the difference in Fermi levels, electrons will flow from MoO_2 (higher Fermi level) to BiOBr (lower Fermi level), until the two Fermi levels reach equilibrium.[45] Negative charges will aggregate on the surface of BiOBr, while positive charges will aggregate on the surface of MoO_2. The rearrangement of electrons in the heterojunction creates a potential difference between them, which leads to the generation of a built-in electric field (BIEF, the direction of the electric field is MoO_2 → BiOBr). Under the action of the BIEF, electrons on the conduction band of BiOBr flow towards the valence band of MoO_2, forming a Z-shaped transmission path (Fig. 6a and 7e), allowing electrons to

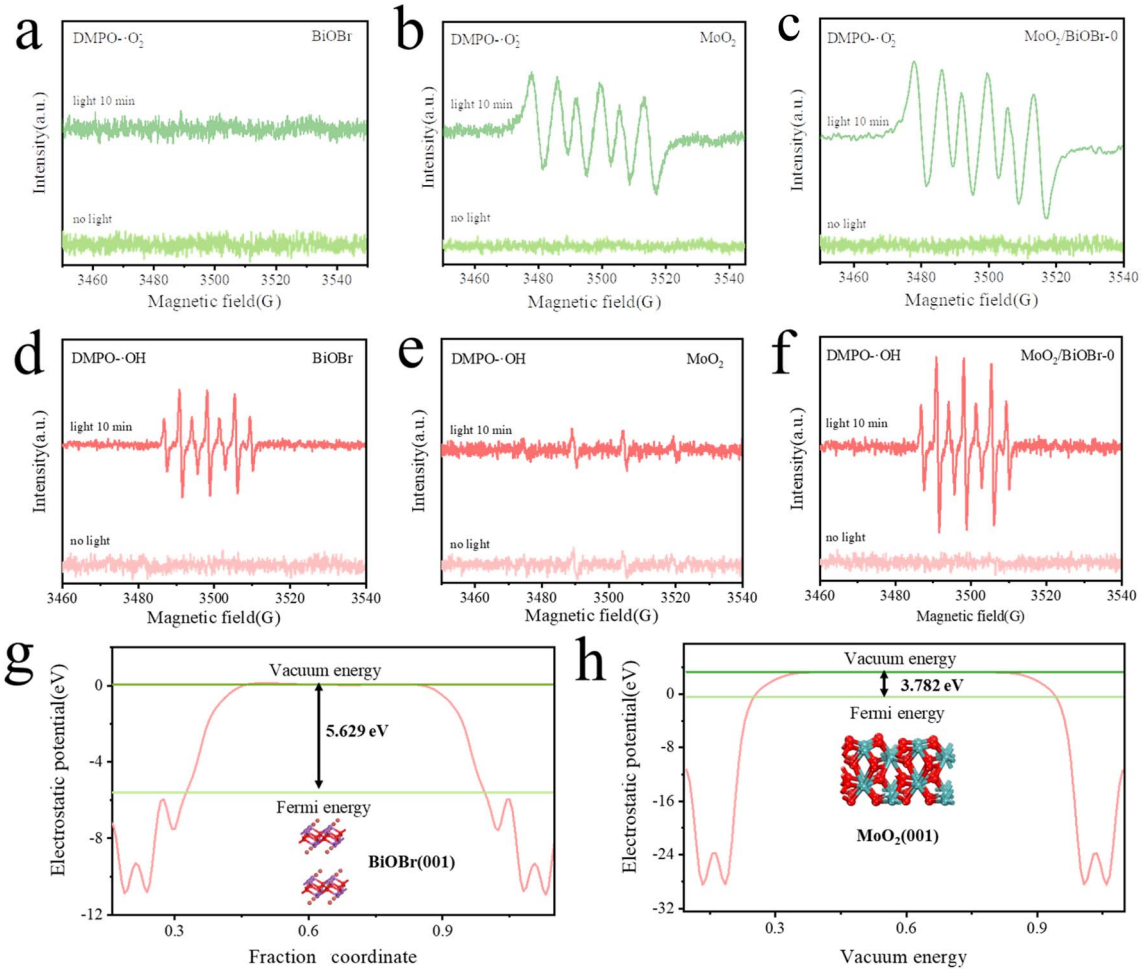

Fig. 5 ESR characterization of DMPO–$\cdot O_2^-$ for (a) BiOBr, (b) MoO_2 and (c) MoO_2/BiOBr-0; ESR characterization of DMPO–$\cdot$OH for (d) BiOBr, (e) MoO_2 and (f) MoO_2/BiOBr-0; electrostatic potential energies of (g) BiOBr and (h) MoO_2.

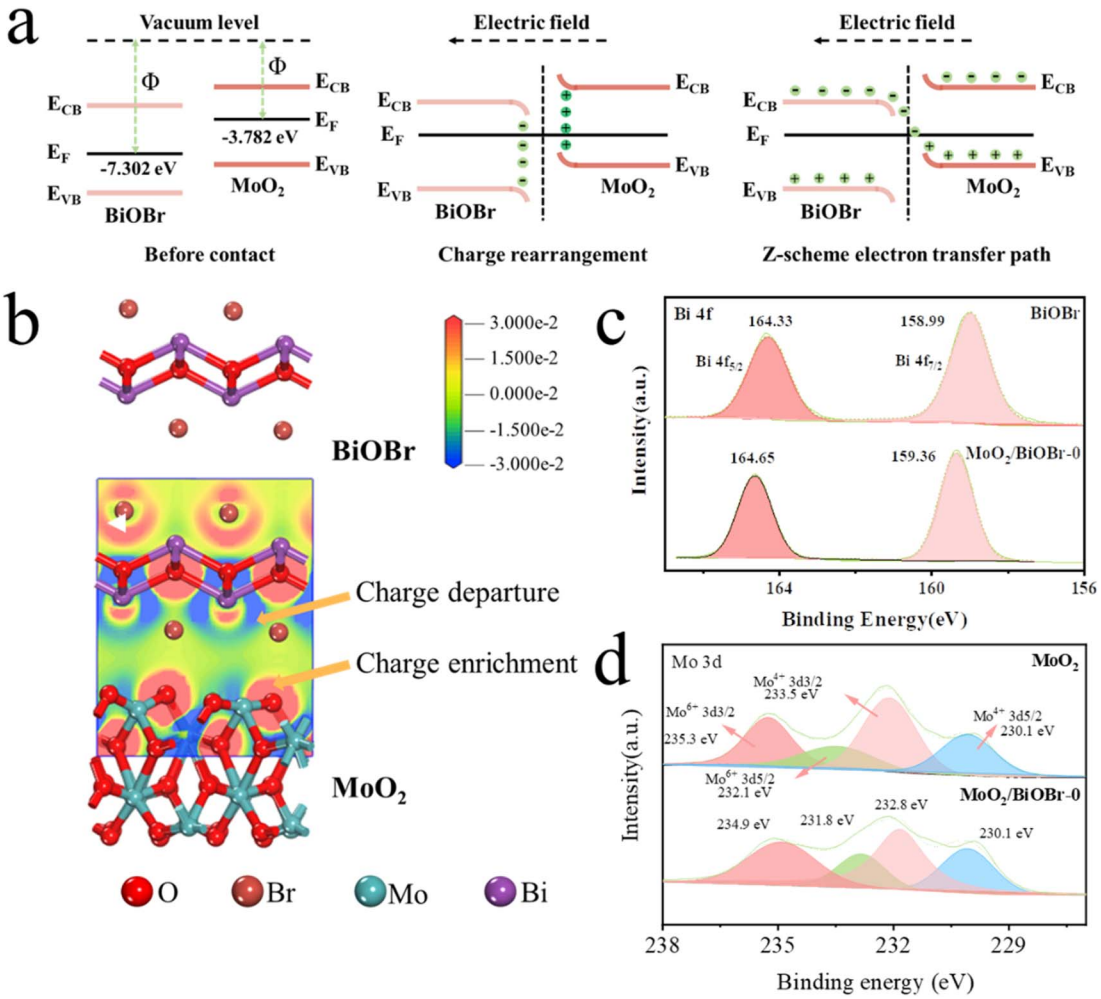

Fig. 6 (a) Diagram of the formation process of the Z-scheme heterojunction; (b) charge difference density diagram; (c) XPS high-resolution spectra of Bi 4f and (d) Mo 3d.

accumulate in the conduction band of MoO_2 and holes to accumulate in the valence band of BiOBr, used for participating in the synthesis of ammonia reaction.

To further demonstrate the charge transfer between BiOBr and MoO_2, the differential charge density of MoO_2/BiOBr was calculated using DFT, as shown in Fig. 6b. The red part in the figure represents the accumulation of charges, while the blue part is the departure of charges, indicating that the electron density on the MoO_2 surface is higher than that of BiOBr, that is, electrons continuously flow from the BiOBr surface to the MoO_2 surface, enriching electrons on MoO_2.[46] The differential charge density proves the existence of electron rearrangement between the two phases of BiOBr and MoO_2 in the Z-scheme heterojunction, and the direction of electron transfer is from BiOBr to MoO_2. As the direction of photo-generated electron transfer induced by the built-in electric field is opposite to the direction of the field strength, this further proves that the direction of the electric field is from MoO_2 to BiOBr.

The variation of binding energy in the XPS high-resolution spectrum is also related to the electron transfer pathway of heterojunctions.[42] Therefore, Bi element in BiOBr and Mo element in MoO_2 were characterized by high-resolution XPS spectroscopy. The XPS spectrum of Bi 4f indicates that the binding energy of Bi $4f_{5/2}$ and Bi $4f_{7/2}$ in BiOBr is 164.33 eV and 158.99 eV (Fig. 6c), respectively, while in MoO_2/BiOBr-0, the binding energy of Bi 4f shifts to 164.65 eV and 159.36 eV, indicating a decrease in electron density on the surface of BiOBr.[47] For Mo 3d (Fig. 6d), there are Mo^{4+} $3d_{5/2}$ and Mo^{4+} $3d_{3/2}$ with Mo^{4+} chemical states, as well as Mo^{6+} $3d_{5/2}$ and Mo^{6+} $3d_{3/2}$ with Mo^{6+} chemical states.[48] Compared with BiOBr, the binding energy of Mo 3d in MoO_2/BiOBr-0 shifts towards a lower value, indicating a decrease in electron density, which means that high electron density is located on the surface of MoO_2. When BiOBr and MoO_2 come into contact to form a heterojunction, electrons will transfer from the surface of BiOBr to MoO_2, and then gather on the surface of MoO_2. The consistency between the characterization of the XPS high-resolution spectrum and the results obtained by DFT also confirms the formation of a built-in electric field after the contact between BiOBr and MoO_2.

3.5.3 Strength of the built-in electric field (BIEF) and efficiency of bulk charge separation (BCS). In order to investigate the differences in photogenerated carrier separation and transfer

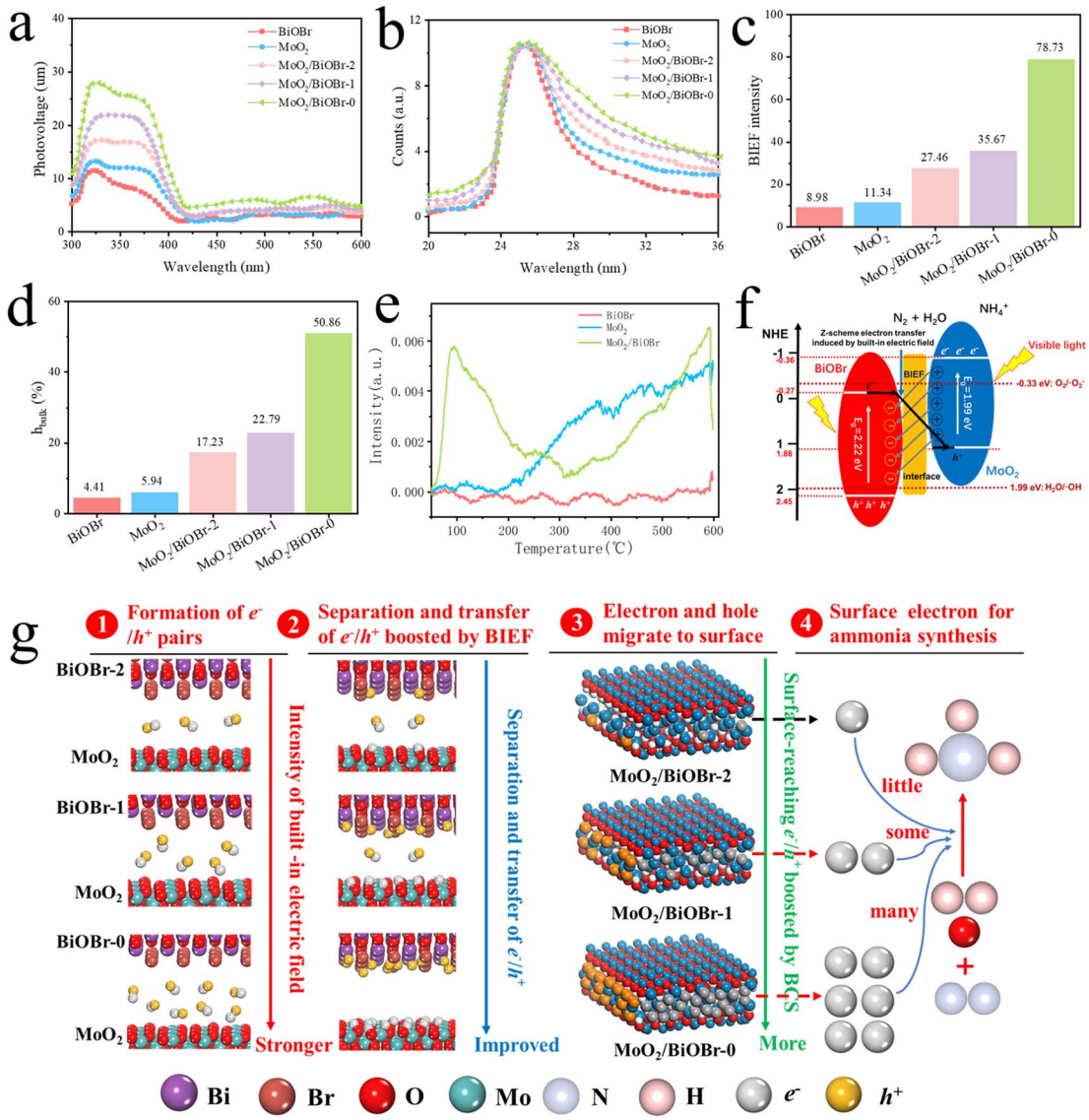

Fig. 7 (a) Surface photovoltage (SPV) test; (b) transient fluorescence spectrum (TRPL) test; (c) built-in electric field (BIEF) intensity; (d) bulk-charge separation (BCS) efficiency (η_{bulk}) for all samples; (e) N_2-TPD characterization; (f) schematic diagram of the built-in electric field (BIEF) in the Z-scheme heterojunction; (g) schematic diagram of the mechanism of photocatalytic ammonia synthesis catalyzed by MoO_2/BiOBr.

in MoO_2/BiOBr Z-scheme heterojunctions with different facet ratios, surface photovoltage spectroscopy (SPV) and transient fluorescence spectroscopy (TRPL) were performed. Fig. 7a shows the SPV results of five samples. The SPV response signals of BiOBr and MoO_2 are relatively low, indicating that the separation effect of photo-generated carriers in this region is not strong. After forming the Z-scheme heterojunction, the SPV signal of MoO_2/BiOBr is significantly enhanced, indicating that the two-phase recombination significantly enhances the charge separation efficiency of the material. More importantly, as the facet ratio of (102)/(001) increases, the SPV response (maximum value) of MoO_2/BiOBr-2, MoO_2/BiOBr-1, and MoO_2/BiOBr-0 increases significantly to 16.9 μV, 21.8 μV and 27.6 μV. The above results indicate that forming a Z-scheme heterojunction can significantly improve the performance of single-phase materials in terms of electron and hole separation and transfer efficiency, and the above performance will significantly increase with the increase of the (102)/(001) ratio.

Fig. 7b and Table S1† show the transient fluorescence spectrum (TRPL) results of the samples. Based on the formulae reported in the literature, the average decay lifetime of electrons generated by the five materials was calculated (τ_{av}).[49,50] The corresponding values for BiOBr, MoO_2, MoO_2/BiOBr-2, MoO_2/BiOBr-1 and MoO_2/BiOBr-0 are 1.76 ns, 2.87 ns, 4.99 ns, 5.75 ns, and 9.14 ns, respectively. It indicates that the MoO_2/BiOBr Z-scheme heterojunction is also significantly stronger in the lifetime of photo-generated electrons compared to single-phase BiOBr and MoO_2, and the value significantly increases with the increase of the (102)/(001) facet ratios.

Through the calculation of the work function, it is known that an internal electric field is formed within the MoO_2/BiOBr heterojunction, which promotes the transfer of photo-

generated electrons along the direction of BiOBr to MoO_2 between the two phases. Previous photoelectric performance tests have shown that the efficiency of charge separation and transfer is MoO_2/BiOBr-0 > MoO_2/BiOBr-1 > MoO_2/BiOBr-2 > MoO_2 > BiOBr. In order to explore its underlying reasons, the changes in the BIEF intensity of these materials were measured using a model developed by Kanata *et al.*,[51] as shown in Fig. 7c. According to the model, the strength of the BIEF is determined by surface voltage and surface charge density. Therefore, the above parameters were measured through open circuit potential testing, simultaneous potentiometric titration, and conductivity titration, and the results are shown in Fig. S8–S10†.[52,53] The BIEF strengths of BiOBr and MoO_2 are only 8.98 and 11.34. After forming a heterojunction, the BIEF value of MoO_2/BiOBr significantly increased to 27.46–78.73. In particular, as the facet ratio of (102)/(001) increases, the BIEF value of the MoO_2/BiOBr heterojunction also increases positively, and the maximum BIEF of MoO_2/BiOBr-0 is 78.73. This fully demonstrates that changing the (102)/(001) ratio can effectively regulate the BIEF intensity of MoO_2/BiOBr heterojunctions. The strength of the BIEF directly affects the transfer of photogenerated electrons and holes, thereby affecting the photocatalytic performance of the photocatalysts.[54]

The bulk charge separation (BCS) efficiency of the five samples was further measured using the equation reported by Kim *et al.*[55] Fig. 7d shows that the BCS efficiencies of BiOBr, MoO_2, MoO_2/BiOBr-2, MoO_2/BiOBr-1 and MoO_2/BiOBr-0 are 4.41%, 5.94%, 17.23%, 22.79%, and 50.86%, respectively. The above results fully demonstrate that increasing the (102)/(001) ratio can effectively increase the BCS efficiency of MoO_2/BiOBr heterojunctions, thereby increasing the number of electrons and holes transferred to the catalyst surface. Thus, based on previous photocatalytic activity results, it can be inferred that facet engineering can regulate the strength of the BIEF in MoO_2/BiOBr, making it more advantageous to obtain high BCS efficiency. This promotes the action of surface enriched photogenerated electrons on nitrogen reduction, thereby achieving efficient photocatalytic ammonia synthesis.

In addition, the adsorption capacity of the catalyst for N_2 was studied using N_2-TPD characterization, which is shown in Fig. 7e. It can be clearly seen that MoO_2/BiOBr-0 has stronger adsorption compared to BiOBr and MoO_2, indicating that the loading of MoO_2 enables BiOBr to have stronger chemical adsorption capacity for N_2 molecules.

3.5.4 Theoretical calculation of the nitrogen reduction path. As shown in Fig. 8a, the different adsorption configurations of nitrogen on the catalyst can lead to the NRR occurring along different reaction pathways.[56,57] When N_2 is adsorbed end-to-end on catalysts, the NRR will follow the distal, alternating, and mixing paths. In the first step of the hydrogenation reaction, the distant N atom will preferentially react to generate *NNH. The distal path (red) is the hydrogenation reaction between the N atom at the far end and the H atom in the first three steps to generate the first NH_3. After the N≡N bond breaks, the adsorbed near end N atom reacts with the three H atoms to generate NH_3. In the alternating path (green), H atoms are alternately added to both ends of N atoms, and the fourth step of the hydrogenation reaction generates an $*NH_2NH_2$ intermediate, which is then further hydrogenated to produce the first NH_3 molecule. When the two ends of the N_2 molecule are adsorbed on catalysts, *i.e.* lateral adsorption, the two N atoms are equal in the first step of the hydrogenation reaction, and the NRR will proceed along enzymatic, consecutive, and mixed pathways. The hydrogenation method of the enzymatic pathway (purple) is the same as that of the alternating pathway, both of which involve sequential hydrogenation at both ends. The consecutive path (blue) is the same as the distal path because the N atom after the first step of hydrogenation may react more easily with the subsequent H atom. The mixed path (black) takes into account the possibility of crossing among the first four paths.

The NRR pathways of MoO_2, BiOBr, and MoO_2/BiOBr were calculated, and the relevant data and Gibbs free energy are shown in Table 1 and Fig. 8. The common reason for limiting the NRR is that the potential energy determination step (PDS) is too high, which prevents the reaction from proceeding normally. According to literature reports and our previous research,[56–58] the first step hydrogenation reaction ($*N_2 + H^+ + e^- = *NNH$) and the last step hydrogenation reaction ($*NH_2 + H^+ + e^- = NH_3$) of the NRR are generally the PDS of the entire reaction.[59,60] The free energies of BiOBr's end and lateral adsorption of N_2 are −0.249 eV and −0.335 eV, respectively, with a small difference. There is no significant competition between the two adsorption configurations. By comparing the PDS of five NRR pathways on BiOBr, it was found that the potential barrier was highest when generating $*NH_2NH_2$ and $*NH_2$ intermediates, and these two hydrogenation reactions were the PDS of the entire reaction. The free energies for generating $*NH_2NH_2$ in alternating and enzymatic pathways are 0.834 eV and 0.869 eV, respectively, while the free energy for generating NH_2 is the highest, in which ΔG_{max} is 1.309 eV (Fig. 8b and c). N_2 tends to perform the NRR along alternating paths on BiOBr, ΔG_{max} is −0.834 eV, the limiting potential U_L is −0.834 V, the free energy is high, and the competitive hydrogen evolution reaction (HER) will dominate, preventing the progress of the NRR. The occurrence of the NRR on MoO_2 exhibits a similar pattern to BiOBr (Fig. 8d and e). The PDS on MoO_2 is also involved in a two-step hydrogenation reaction to generate $*NH_2NH_2$ and $*NH_2$ intermediates, with the difference being that the free energy is reduced, making the reaction easier to proceed. The lowest free energy for the enzymatic pathway to generate the $*NH_2NH_2$ intermediate is 0.635 eV, which is 0.199 eV lower than the alternative pathway of BiOBr to generate $*NH_2NH_2$. The free energy (ΔG_{max}) of NH_2 intermediates generated by distal and consecutive pathways on MoO_2 is 1.062 eV, and an excessively high PDS prevents the progress of these two paths. Compared to BiOBr, the U_L of MoO_2 is −0.635 V, which has been reduced to a certain extent, but the competitive HER will still dominate. The weak adsorption of N_2 on BiOBr and MoO_2, strong competitive adsorption of H, and the high PDS indicate that these two catalysts cannot effectively catalyze the NRR.

The adsorption free energy of MoO_2/BiOBr for N_2 reached −0.907 eV and −0.888 eV, indicating a significant improvement in adsorption capacity. In the distal pathway of the NRR, the first step hydrogenation reaction of MoO_2/BiOBr generates

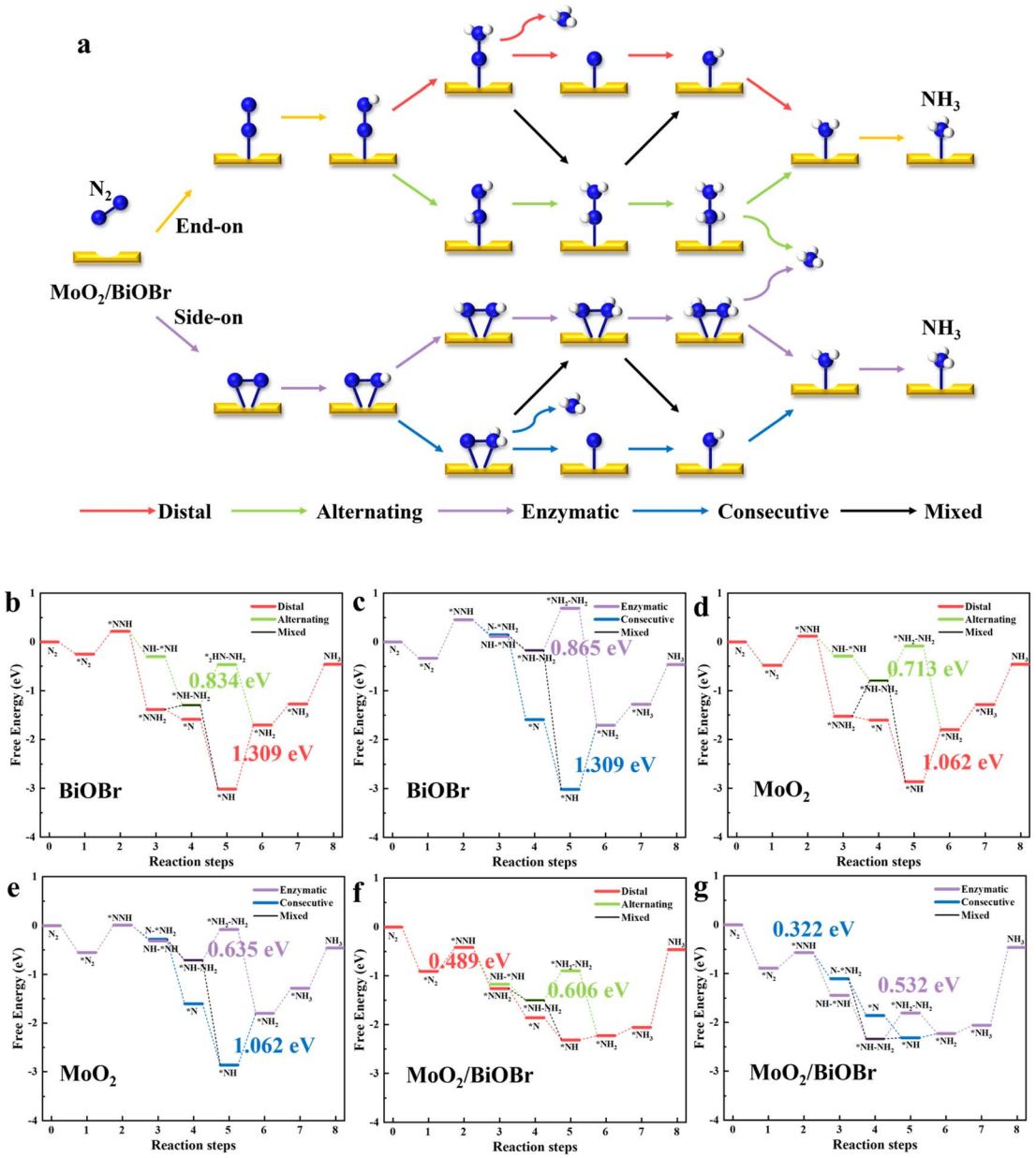

Fig. 8 (a) Schematic diagram of various reaction pathways for nitrogen reduction to synthesize ammonia; free energy diagrams for the five reaction paths on (b and c) BiOBr, (d and e) MoO_2 and (f and g) MoO_2/BiOBr. Note: the numbers in the diagrams are the values of the potential decision step (PDS).

a free energy (ΔG_{max}) of 0.489 eV for the *NNH intermediate, which is the PDS of this path (Fig. 8f). The PDS of alternating paths also appears in the generation of $*NH_2NH_2$ intermediates, with a PDS of 0.606 eV (Fig. 8f). When N_2 is laterally adsorbed on MoO_2/BiOBr, the first step of the hydrogenation reaction is the PDS of consecutive and mixed paths with a free energy (ΔG_{max}) of 0.322 eV (Fig. 8g). The enzymatic pathway involves the generation of $*NH_2NH_2$ intermediates with a free energy (ΔG_{max}) is 0.532 eV. MoO_2/BiOBr tends to undergo the NRR along both consecutive and mixed pathways, with a U_L of only −0.322 V, and a lower limiting potential allowing the reaction to proceed more efficiently.

A comprehensive comparison of MoO_2, BiOBr and MoO_2/BiOBr reveals that for the two single-phase materials, the generation of $*NH_2NH_2$ intermediates is more difficult and requires more energy. After the formation of a Z-scheme heterojunction, the step of limiting the potential changes to generate the first step *NNH, indicating that there are more positions on the surface to accommodate the intermediate $*NH_2NH_2$, making the reaction proceed better. MoO_2/BiOBr not only exhibits stronger adsorption of N_2 than H, but also free energy (ΔG_{max}) is low, exhibiting excellent NRR activity. The calculated data are completely consistent with the experimental results, further confirming that constructing a Z-scheme

Table 1 Gibbs free energies for the NRR paths on MoO_2, BiOBr and MoO_2/BiOBr

	Gibbs free energies (ΔG, eV)		
Reaction steps	BiOBr	MoO_2	MoO_2/BiOBr
Distal			
R1: $N_2 + * = *N_2$	−0.249	−0.481	−0.907
R2: $*N_2 + H^+ + e^- = *NNH$	0.217	0.119	−0.418
R3: $*NNH + H^+ + e^- = *NNH_2$	−1.387	−1.529	−1.260
R4: $*NNH_2 + H^+ + e^- = *N + NH_3$	−1.590	−1.604	−1.859
R5: $*N + H^+ + e^- = *NH$	−3.017	−2.864	−2.317
R6: $*NH + H^+ + e^- = *NH_2$	−1.708	−1.802	−2.230
R7: $*NH_2 + H^+ + e^- = *NH_3$	−1.277	−1.284	−2.059
Alternating			
R3: $*NNH + H^+ + e^- = *NHNH$	−0.301	−0.291	−1.171
R4: $*NHNH + H^+ + e^- = *NHNH_2$	−1.298	−0.794	−1.504
R5: $*NHNH_2 + H^+ + e^- = *NH_2NH_2$	−0.464	−0.081	−0.898
R6: $*NH_2NH_2 + H^+ + e^- = *NH_2 + NH_3$	−1.708	−1.802	−2.230
Enzymatic			
R1: $N_2 + * = *N_2$	−0.335	−0.551	−0.888
R2: $*N_2 + H^+ + e^- = *NNH$	0.456	0.014	−0.566
R3: $*NNH + H^+ + e^- = *NHNH$	0.114	−0.310	−1.445
R4: $*NHNH + H^+ + e^- = *NHNH_2$	−0.173	−0.712	−2.339
R5: $*NHNH_2 + H^+ + e^- = *NH_2NH_2$	0.691	−0.076	−1.807
R6: $*NH_2NH_2 + H^+ + e^- = *NH_2 + NH_3$	−1.708	−1.802	−2.230
Consecutive			
R3: $N*NH + H^+ + e^- = N*NH_2$	0.148	−0.282	−1.106
R4: $N*NH_2 + H^+ + e^- = *N + NH_3$	−1.590	−1.604	−1.859
Total: $N_2 + 6H^+ + 6e^- = 2NH_3$	−0.460	−0.460	−0.460

heterojunction can greatly promote the performance of MoO_2 and BiOBr in catalyzing nitrogen reduction to synthesize ammonia.

3.6. Summary of the mechanism of photocatalytic nitrogen reduction

Based on the experimental results and theoretical calculations mentioned above, a mechanism was proposed to enhance the photocatalytic nitrogen reduction activity of heterojunctions by controlling the facet ratio and adjusting the BIEF intensity (Fig. 7g):

Firstly, MoO_2 and BiOBr form a Z-scheme heterojunction, and due to the difference in Fermi energy levels, a built-in electric field is formed between MoO_2 and BiOBr.

Secondly, in heterojunctions, the BIEF drives electron and hole transfer and accumulates on MoO_2 and BiOBr, respectively. Increasing the (102)/(001) facet ratio of BiOBr nanosheets can enhance the strength of the heterojunction's BIEF.

Furthermore, the strength of the BIEF determines the efficiency of electron migration to the catalyst surface for ammonia synthesis. That is to say, higher BIEF intensity has a greater surface charge separation efficiency (BCS), allowing the separated electrons to better migrate from the bulk to the surface of MoO_2 for photocatalytic synthesis of ammonia, thereby obtaining higher activity.

Finally, compared to MoO_2 and BiOBr, MoO_2/BiOBr not only adsorbs N_2 more strongly than H, but ΔG_{max} is also lower, thus exhibiting superior NRR activity. The calculated data are completely consistent with the experimental results, further confirming that the construction of heterojunctions greatly promotes the performance of MoO_2 and BiOBr in catalyzing nitrogen reduction. The activity increases with the increase of the (102)/(001) ratio of BiOBr nanosheets in the MoO_2/BiOBr heterojunction.

4. Conclusions

This paper presents a MoO_2/BiOBr Z-scheme heterojunction formed by loading MoO_2 on BiOBr nanosheets with different facet ratios, for photocatalytic nitrogen reduction synthesis of ammonia. The Z-scheme heterojunction mechanism of the catalyst was demonstrated through UV-visible diffuse reflection, ESR characterization, and DFT calculations. The catalytic activity results indicate that as the (102)/(001) ratio of BiOBr increases, the photocatalytic activity of the MoO_2/BiOBr Z-scheme heterojunction for nitrogen reduction to ammonia synthesis gradually increases, reaching a maximum of 176.66 $\mu mol\ g^{-1}\ h^{-1}$. Due to the increase in the (102)/(001) facet ratio, the BIEF strength between the two phases of the heterojunction is enhanced, resulting in a high BCS efficiency. This promotes more surface enriched photo-generated electrons to act on nitrogen reduction, thereby achieving efficient photocatalytic nitrogen reduction for ammonia synthesis. The theoretical calculation results of the nitrogen reduction pathway indicate that compared to MoO_2 and BiOBr, MoO_2/BiOBr not only adsorbs N_2 more strongly than H, but also ΔG_{max} is lower, thus exhibiting superior NRR activity. The calculated data are completely consistent with the experimental results, further confirming that the construction of heterojunctions greatly promotes the performance of MoO_2 and BiOBr in catalyzing nitrogen reduction. This work combines facet engineering and Z-scheme heterojunctions, providing guidance and reference for constructing efficient photocatalysts for catalyzing nitrogen to ammonia.

Conflicts of interest

There are no conflicts to declare.

Acknowledgements

This work is supported by the National Natural Science Foundation of China (22278371, 92061126, and 22378110).

References

1 Y. R. Tian, H. T. Tan, X. Li, J. J. Jia, Z. X. Mao, J. Liu and J. Liang, Metal-based electrocatalysts for ammonia electrooxidation reaction to nitrate/nitrite: past, present, and future, *Chin. J. Catal.*, 2024, **56**, 25–50.

2 G. H. Zhang, X. Q. Zhang, Y. Meng, G. X. Pan, Z. M. Ni and S. J. Xia, Layered double hydroxides–based photocatalysts in visible-light photodegradation of organic pollutants: a review, *Chem. Eng. J.*, 2020, **392**, 123684.

3 M. A. Mushtaq, A. Kumar, W. Liu, Q. Q. Ji, Y. G. Deng, G. Yasin, A. Saad, W. Raza, J. Zhao, S. Ajmal, Y. Y. Wu, M. Ahmad, N. R. Lashari, Y. Wang, T. S. Li, S. J. Sun, D. D. Zheng, Y. S. Luo, X. K. Cai and X. P. Sun, A metal coordination number determined catalytic performance in manganese borides for ambient electrolysis of nitrogen to ammonia, *Adv. Mater.*, 2024, 2313086.

4 L. Cai, J. R. Guo, T. Liu, J. Tian, Z. L. Wang, Y. Liu, M. S. Hamdy and X. P. Sun, Selective photo-reduction of nitrate to nitrogen with a two-step process by a KBH_4/Cu(II) modified $CuFe_2O_4$ photocatalyst, *Nano Res.*, 2023, **16**, 10462–10475.

5 G. M. Ren, J. Y. Zhao, Z. H. Zhao, Z. Z. Li, L. Wang, Z. S. Zhang, C. H. Li and X. C. Meng, Defects-induced single-atom anchoring on metal-organic frameworks for high-efficiency photocatalytic nitrogen reduction, *Angew. Chem., Int. Ed.*, 2023, **63**, e202314408.

6 L. Ouyang, J. Liang, Y. S. Luo, D. D. Zheng, S. J. Sun, Q. Liu, M. S. Hamdy, X. P. Sun and B. W. Ying, Recent advances in electrocatalytic ammonia synthesis, *Chin. J. Catal.*, 2023, **50**, 6–44.

7 X. L. Song, L. Chen, L. J. Gao, J. T. Ren and Z. Y. Yuan, Engineering g-C_3N_4 based materials for advanced photocatalysis: recent advances, *Green Energy Environ.*, 2024, **9**, 166–197.

8 Y. T. Sun, B. K. Xia, S. Ding, L. C. Yu, S. Chen and J. J. Duan, Rigid two-dimensional indium metal–organic frameworks boosting nitrogen electroreduction at all pH values, *J. Mater. Chem. A*, 2021, **9**, 20040–20047.

9 H. J. Chen, Z. Q. Xu, S. J. Sun, Y. S. Luo, Q. Liu, M. S. Hamdy, Z. S. Feng, X. P. Sun and Y. Wang, Plasma-etched Ti_2O_3 with oxygen vacancies for enhanced NH_3 electrosynthesis and Zn–N_2 batteries, *Inorg. Chem. Front.*, 2022, **9**, 4608–4613.

10 H. B. Yin, Z. Chen, Y. Peng, S. C. Xiong, Y. D. Li, H. Yamashita and J. H. Li, Dual active centers bridged by oxygen vacancies of ruthenium single-atom hybrids supported on molybdenum oxide for photocatalytic ammonia synthesis, *Angew. Chem., Int. Ed.*, 2022, **133**, e202114242.

11 B. B. Guo, X. Y. Cheng, Y. Tang, W. Guo, S. Q. Deng, L. Wu and X. Z. Fu, Dehydrated UiO-66$(SH)_2$: The Zr-O cluster and its photocatalytic role mimicking the biological nitrogen fixation, *Angew. Chem., Int. Ed.*, 2022, **61**, e202117244.

12 S. T. Liu, G. M. Ren and X. C. Meng, BrO_3^- bridge Bi_2O_3/$Bi(OH)_3$ heterojunction with multiple charge transfer channels for efficient photocatalytic nitrogen fixation and CO_2 reduction, *ACS Sustain. Chem. Eng.*, 2024, **11**, 15599–15608.

13 S. Ghoshal, A. Ghosh, P. Roy, B. Ball, A. Pramanik and P. Sarkar, Recent progress in computational design of single-atom/cluster catalysts for electrochemical and solar-driven N_2 fixation, *ACS Catal.*, 2022, **12**, 15541–15575.

14 Q. Li, Y. N. Liu, Z. Wan, H. Y. Cao, S. Zhang, Y. Zhou, X. Y. Ye, X. Y. Liu and D. Q. Zhang, Microwave-assisted synthesis of oxygen vacancy associated TiO_2 for efficient photocatalytic nitrate reduction, *Chin. Chem. Lett.*, 2022, **33**, 3835–3841.

15 G. J. Dong, X. J. Huang and Y. P. Bi, Anchoring black phosphorus quantum dots on Fe-doped $W_{18}O_{49}$ nanowires for efficient photocatalytic nitrogen fixation, *Angew. Chem., Int. Ed.*, 2022, **61**, e202204271.

16 Q. Li, Y. Q. Jiao, Y. Q. Tang, J. Zhou, B. G. Wu, B. J. Jiang and H. G. Fu, Shear stress triggers ultrathin-nanosheet carbon nitride assembly for photocatalytic H_2O_2 production coupled with selective alcohol oxidation, *J. Am. Chem. Soc.*, 2023, **145**, 20837–20848.

17 L. Ju, Y. D. Ma, X. Tan and L. Z. Kou, Controllable electrocatalytic to photocatalytic conversion in ferroelectric heterostructures, *J. Am. Chem. Soc.*, 2023, **145**, 26393–26402.

18 L. Y. Zhang, Z. L. Huang, B. Xie and S. J. Xia, Experimental and theoretical research on photocatalytic nitrogen reduction using MoS_2 nanosheets with polysulfide vacancies, *Inorg. Chem.*, 2024, **63**(23), 10871–10880.

19 C. Y. Feng, Z. P. Wu, K. W. Huang, J. H. Ye and H. B. Zhang, Surface modification of 2D photocatalysts for solar energy conversion, *Adv. Mater.*, 2022, **34**, 2200180.

20 H. P. Li, G. A. Wang, Q. H. Deng, W. X. Hu and W. G. Hou, Metal-alcohol coordination promoted reduction of bismuth (III) in bismuth-based semiconductors for enhanced photocatalytic activity, *Appl. Catal., B*, 2024, **344**, 123652.

21 S. S. Shang, W. Xiong, C. Yang, B. Johannessen, R. G. Liu, H. Y. Hsu, Q. F. Gu, M. K. H. Leung and J. Shang, Atomically dispersed iron metal site in a porphyrin-based metal-organic framework for photocatalytic nitrogen fixation, *ACS Nano*, 2021, **15**, 9670–9678.

22 L. H. Lin, Z. Y. Lin, J. Zhang, X. Cai, W. Lin, Z. Y. Yu and X. C. Wang, Molecular–level insights on the reactive facet of carbon nitride single crystals photocatalysing overall water splitting, *Nat. Catal.*, 2020, **3**, 649–655.

23 L. F. Wei, C. L. Yu, Q. H. Zhang, H. Liu and Y. Wang, TiO_2-based heterojunction photocatalysts for photocatalytic reduction of CO_2 into solar fuels, *J. Mater. Chem. A*, 2018, **6**, 22411–22436.

24 Y. A. Wu, I. McNulty, C. Liu, K. C. Lau, Q. Liu, A. P. Paulikas, C. J. Sun, Z. H. Cai, J. R. Guest, Y. Ren, V. Stamenkovic, L. A. Curtiss, Y. Z. Liu and T. Rajh, Facet-dependent active sites of a single Cu_2O particle photocatalyst for CO_2 reduction to methanol, *Nat. Energy*, 2019, **4**, 957–968.

25 J. Li, L. J. Cai, J. Shang, Y. Yu and L. Z. Zhang, Giant enhancement of internal electric field boosting bulk charge separation for photocatalysis, *Adv. Mater.*, 2016, **28**, 4059–4064.

26 C. Cheng, B. W. He, J. J. Fan, B. Cheng, S. W. Cao and J. G. Yu, An inorganic/organic S–scheme heterojunction H_2–production photocatalyst and its charge transfer mechanism, *Adv. Mater.*, 2021, **33**, 2100317.

27 X. X. Yuan, Z. L. Huang, J. H. Li, Y. Meng, Z. H. Gu, B. Xie, Z. M. Ni and S. J. Xia, The S—Cu—O bonds boosted efficient photocatalytic degradation of semi-coherent interface Cu_2O/Cu_7S_4 heterojunction, *Sep. Purif. Technol.*, 2023, **306**, 122689.

28 X. Li, Y. Meng, W. Shi, B. Xie, Z. M. Ni and S. J. Xia, Construction of high reduction potential Fe-POMs/LDHs Z-

scheme heterojunction: variable valence state-assisted photocatalytic activation of persulfate radical for synergistic degradation of tetracycline, *Mater. Res. Bull.*, 2024, **170**, 112591.

29 J. Z. Qin, X. Hu, X. Y. Li, Z. F. Yin, B. J. Liu and K. H. Lam, 0D/2D $AgInS_2$/MXene Z-scheme heterojunction nanosheets for improved ammonia photosynthesis of N_2, *Nano Energy*, 2019, **61**, 27–35.

30 G. H. Zhang, X. X. Yuan, B. Xie, Y. Meng, Z. M. Ni and S. J. Xia, S Vacancies act as a bridge to promote electron injection from Z–scheme heterojunction to nitrogen molecule for photocatalytic ammonia synthesis, *Chem. Eng. J.*, 2022, **433**, 133670.

31 Y. Shiraishi, M. Hashimoto, K. Chishiro, K. Moriyama, S. Tanaka and T. Hirai, Photocatalytic dinitrogen fixation with water on bismuth oxychloride in chloride solutions for solar–to–chemical energy conversion, *J. Am. Chem. Soc.*, 2020, **142**, 7574–7583.

32 J. Y. Yang, Z. L. Huang, Y. Meng, Z. M. Ni, B. Xie and S. J. Xia, Experimental and theoretical study on photocatalytic nitrogen reduction catalyzed by Fe-doped MoO_2, *Sep. Purif. Technol.*, 2023, **318**, 24019.

33 Z. Ali, J. Ma, M. Hong and R. C. Sun, Review: applications of the functional photocatalysts BiOX (X=Cl, Br, I) for clean energy, the environment, and future photobiorefineries, *J. Mater. Chem. A*, 2023, **11**, 3297–3314.

34 S. H. Lee, H. Nishi and T. Tatsuma, Plasmon-induced charge separation based on a nanocomposite containing MoO_2 under visible light irradiation, *J. Mater. Chem. C*, 2021, **9**, 6395–6398.

35 G. M. Ren, S. T. Liu, M. Shi, Z. S. Zhang, Z. Z. Li and X. C. Meng, Ultraviolet light-modulated defects on BiOBr to improve the photocatalytic fixation of nitrogen to ammonia, *Sol. RRL*, 2022, **6**, 2200653.

36 H. J. W. Li, H. M. Zhou, K. J. Chen, K. Liu, S. Li, K. X. Jiang, W. H. Zhang, Y. B. Xie, Z. Cao, H. Li, H. Liu, X. W. Xu, H. Pan, J. H. Hu, D. S. Tang, X. Q. Qiu, J. W. Fu and M. Liu, Metallic MoO_2-modified graphitic arbon nitride boosting photocatalytic CO_2 reduction via Schottky junction, *Sol. RRL*, 2019, **4**, 1900416.

37 Y. Q. Zheng, M. X. Sun, W. B. Sun, X. L. Meng, X. Z. Huang and Z. Y. Li, Nitrogen–doped graphyne/BiOBr nanocomposites: in situ sonochemical synthesis and boosted photocatalytic performance, *Sep. Purif. Technol.*, 2022, **301**, 122062.

38 H. J. Liu, B. J. Wang, M. Chen, H. Zhang, J. B. Peng, L. Ding and W. F. Wang, Simple synthesis of BiOAc/BiOBr heterojunction composites for the efficient photocatalytic removal of organic pollutants, *Sep. Purif. Technol.*, 2021, **261**, 118286.

39 J. Z. Meng, Y. Y. Duan, S. J. Jing, J. P. Ma, K. W. Wang, K. Zhou, C. G. Ban, Y. Wang, B. H. Hu, D. M. Yu, L. Y. Gan and X. Y. Zhou, Facet junction of BiOBr nanosheets boosting spatial charge separation for CO_2 photoreduction, *Nano Energy*, 2022, **92**, 106671.

40 S. Z. Andersen, V. Čolić, S. Yang, J. A. Schwalbe, A. C. Nielander, J. M. McEnaney, K. Enemark-Rasmussen, J. G. Baker, A. R. Singh, B. A. Rohr, M. J. Statt, S. J. Blair, S. Mezzavilla, J. Kibsgaard, P. C. K. Vesborg, M. Cargnello, S. F. Bent, T. F. Jaramillo, I. E. L. Stephens, J. K. Nørskov and I. Chorkendorff, A Rigorous Electrochemical Ammonia Synthesis Protocol with Quantitative Isotope Measurements, *Nature*, 2019, **570**, 504–508.

41 G. H. Zhang, Y. Meng, B. Xie, Z. M. Ni, H. F. Lu and S. J. Xia, Precise location and regulation of active sites for highly efficient photocatalytic synthesis of ammonia by facet-dependent $BiVO_4$ single crystals, *Appl. Catal., B*, 2021, **296**, 120379.

42 H. Yang, K. Dai, J. F. Zhang and G. Dawson, Inorganic-organic hybrid photocatalysts: syntheses, mechanisms, and applications, *Chin. J. Catal.*, 2022, **43**, 2111–2140.

43 G. H. Zhang, T. T. Dai, Y. Meng, B. Xie, Z. M. Ni and S. J. Xia, Modulation of photo-generated solvated electrons for ammonia synthesis via facet-dependent engineering of heterojunctions, *Appl. Catal., B*, 2021, **288**, 119990.

44 X. S. Zhao, Y. Y. You, S. B. Huang, Y. X. Wu, Y. Y. Ma, G. Zhang and Z. H. Zhang, Z-scheme photocatalytic production of hydrogen peroxide over $Bi_4O_5Br_2$/g-C_3N_4 heterostructure under visible light, *Appl. Catal., B*, 2020, **278**, 119251.

45 T. T. Dai, Z. Y. Yuan, Y. Meng, B. Xie, Z. M. Ni and S. J. Xia, Performance and mechanism of photocatalytic degradation of tetracycline by Z-scheme heterojunction of CdS@LDHs, *Appl. Clay Sci.*, 2021, **221**, 106210.

46 Z. C. Lian, M. H. Qu, H. Xiao, L. H. Wang, H. X. Wu, J. Z. Zi, W. Wang and H. X. Li, Direct observation of Z-Scheme route in $Cu_{31}S_{16}/Zn_xCd_{1-x}S$ heteronanoplates for highly efficient photocatalytic hydrogen evolution, *Small*, 2024, 2400611.

47 Y. P. Zhang, P. Y. Cao, X. H. Zhu, B. Z. Li, Y. F. He, P. F. Song and R. M. Wang, Facile construction of BiOBr ultra-thin nano-roundels for dramatically enhancing photocatalytic activity, *J. Environ. Manag.*, 2021, **299**, 113636.

48 C. B. Bie, B. C. Zhu, L. Wang, H. G. Yu, C. H. Jiang, T. Chen and J. G. Yu, A bifunctional CdS/MoO_2/MoS_2 catalyst enhances photocatalytic H_2 evolution and pyruvic acid synthesis, *Angew. Chem., Int. Ed.*, 2022, **61**, e202212045.

49 P. Lefebvre, J. Allègre, B. Gil and H. Mathieu, Time-resolved photoluminescence as a probe of internal electric fields in GaN-(GaAl)N quantum wells, *Phys. Rev. B: Condens. Matter Mater. Phys.*, 1999, **59**, 15363–15367.

50 G. Morello, S. F. Della, L. Carbone, L. Manna, G. Maruccio, R. Cingolani and M. D. Giorgi, Intrinsic optical nonlinearity in colloidal seeded grown CdSe/CdS nanostructures: photoinduced screening of the internal electric field, *Phys. Rev. B: Condens. Matter Mater. Phys.*, 2008, **78**, 195313.

51 T. Kanata, M. Matsunaga, H. Takakura, Y. Hamakawa and T. Nishino, *Proc. SPIE*, 1990, **56**, 1286.

52 R. Li, J. H. Hu, M. S. Deng, H. L. Wang, X. J. Wang, Y. L. Hu, H.-L. Jiang, J. Jiang, Q. Zhang, Y. Xie and Y. J. Xiong, Integration of an inorganic semiconductor with a metal-organic framework: a platform for enhanced gaseous photocatalytic reactions, *Adv. Mater.*, 2014, **26**, 4783–4788.

53 A. G. S. Prado, L. B. Bolzon, C. P. Pedroso, A. O. Moura and L. L. Costa, Nb_2O_5 as efficient and recyclable photocatalyst for indigo carmine degradation, *Appl. Catal., B*, 2008, **82**, 219–224.

54 Z. Y. Yuan, Y. Y. Cao, Y. Meng, G. X. Pan, Y. F. Zheng, Z. M. Ni and S. J. Xia, The construction of lattice-matched CdS-Ag_2S heterojunction photocatalysts: high-intensity built-in electric field effectively boosts bulk-charge separation efficiency, *J. Hazard. Mater.*, 2023, **485**, 131895.

55 T. W. Kim and K. S. Choi, Nanoporous $BiVO_4$ photoanodes with dual-layer oxygen evolution catalysts for solar water splitting, *Science*, 2014, **343**, 990–994.

56 Z. F. Yang, Y. Meng, B. Xie, Z. M. Ni and S. J. Xia, The structural stability and mechanism of ammonia synthesis of single layer CdS doped by 13 transition metal: first-principles study, *Fuel*, 2024, **355**, 129406.

57 W. L. Zhao, Z. L. Huang, H. Shen, X. L. Li, S. F. Zhao, B. Xie and S. J. Xia, Density functional theory study of CO_2 adsorption on transition metal (M=Al, Li, K, Ca) doped MgO, *Mol. Catal.*, 2024, **553**, 113708.

58 S. J. Xia, Z. Y. Yuan, Y. Meng, C. Zhang, X. L. Li, Z. M. Ni and X. Q. Zhang, Fabrication of site activated and synergistic dual vacancies $ZnIn_2S_4$ for highly efficient bifunctional photocatalysis: nitrogen reduction and oxidative degradation, *J. Mater. Chem. A*, 2024, **12**, 2294–2308.

59 S. Zhang, Y. X. Zhao, R. Shi, C. Zhou, G. I. N. Waterhouse, L. Z. Wu, C. H. Tung and T. R. Zhang, Efficient photocatalytic nitrogen fixation over $Cu^{\delta+}$-modified defective ZnAl-layered double hydroxide nanosheets, *Adv. Energy Mater.*, 2020, **10**, 1901973.

60 C. He, C. Xu and W. X. Zhang, Shortening the screening process towards high-performance 2D-MOF NRR electrocatalysts with $\Delta(\mu_{B\_TM}\text{-}\mu_{B\_X})$ as the descriptor of N_2 activation capability, *Appl. Surf. Sci.*, 2022, **606**, 154904.